



CHORUS

This is the accepted manuscript made available via CHORUS. The article has been published as:

Anomalous Nernst Effect in the Dirac Semimetal $\text{Cd}_{3}\text{As}_{2}$

Tian Liang, Jingjing Lin, Quinn Gibson, Tong Gao, Max Hirschberger, Minhao Liu, R. J. Cava,
and N. P. Ong

Phys. Rev. Lett. **118**, 136601 — Published 29 March 2017

DOI: [10.1103/PhysRevLett.118.136601](https://doi.org/10.1103/PhysRevLett.118.136601)

Anomalous Nernst Effect in the Dirac Semimetal Cd₃As₂

Tian Liang^{1*,†}, Jingjing Lin^{1*}, Quinn Gibson², Tong Gao¹,

Max Hirschberger¹, Minhao Liu¹, R. J. Cava², and N. P. Ong¹

Departments of Physics¹ and Chemistry², Princeton University, Princeton, NJ 08544

(Dated: February 28, 2017)

Dirac and Weyl semimetals display a host of novel properties. In Cd₃As₂, the Dirac nodes lead to a protection mechanism that strongly suppresses backscattering in zero magnetic field, resulting in ultrahigh mobility ($\sim 10^7 \text{ cm}^2 \text{ V}^{-1} \text{ s}^{-1}$). In applied magnetic field, an anomalous Nernst effect is predicted to arise from the Berry curvature associated with the Weyl nodes. We report observation of a large anomalous Nernst effect in Cd₃As₂. Both the anomalous Nernst signal and transport relaxation time τ_{tr} begin to increase rapidly at $\sim 50 \text{ K}$. This suggests a close relation between the protection mechanism and the anomalous Nernst effect. In a field, the quantum oscillations of bulk states display a beating effect, suggesting that the Dirac nodes split into Weyl states, allowing the Berry curvature to be observed as an anomalous Nernst effect.

The field of topological quantum materials has recently expanded to include the Dirac (and Weyl) semimetals, which feature 3D bulk Dirac states with nodes that are protected by symmetry [1–4]. In Dirac semimetals, each Dirac cone is the superposition of two Weyl nodes which have opposite chiralities ($\chi = \pm 1$). The Weyl nodes are prevented from hybridizing by the combination of point group symmetry, inversion symmetry and time-reversal symmetry (TRS) [4]. In the presence of a magnetic field \mathbf{B} , the breaking of TRS leads to separation of the Weyl nodes and the appearance of a Berry curvature $\mathbf{\Omega}(\mathbf{k})$. Because $\mathbf{\Omega}(\mathbf{k})$ acts like an intense magnetic field, it exerts a strong force on charge carriers [5, 6]. The first examples of Dirac semimetals, Na₃Bi and Cd₃As₂, were identified by Wang *et al.* [7, 8]. (In the Weyl semimetal TaAs, the Weyl nodes are already well separated in zero \mathbf{B} because its space group lacks inversion symmetry. The signature surface Fermi arcs were recently observed by angle-resolved photoemission experiments on TaAs [9–11]. Surface modes in Cd₃As₂ have also been observed by Shubnikov de Haas (SdH) oscillations [12].)

An interesting phenomenon in Dirac and Weyl semimetals is the chiral anomaly which refers to the axial current that results from “pumping” electrons between left- and right-moving Dirac branches (of opposite χ) when an electric field \mathbf{E} is applied $\parallel \mathbf{B}$ [13–16]. Recently, the chiral anomaly was successfully observed as a large, negative longitudinal magnetoresistance (LMR) in Na₃Bi [17] and GdPtBi [18]. The anomaly engenders a 4- to 6-fold decrease in the longitudinal resistance in a moderate B . Negative LMRs have also been reported in Bi_{1-x}Sb_x [19], Cd₃As₂ [20, 21], ZrTe₅ [22], TaAs [23].

Quite distinct from the chiral anomaly, the Berry curvature arising from separation of the Weyl nodes leads to other unusual transport effects, particularly the anomalous Hall effect (AHE) and the anomalous Nernst effect (ANE) [24, 25]. Unlike conventional system, no ferromagnetism is required for the AHE and ANE in Dirac semimetals because of the strong Berry curvature emanated by Weyl nodes. The anomalous Hall conductivity

is expressed as [3, 26],

$$\sigma_{\text{AHE}} = \frac{e^2}{2\pi\hbar} \left| \sum \Delta \mathbf{k}_i \right| \quad (1)$$

where $\Delta \mathbf{k}_i$ is the distance between the i^{th} pair of Weyl nodes. The thermopower and Nernst effect in Weyl semimetals has been calculated in the Boltzmann equation approach [27–30].

We report measurements of the thermoelectric tensor S_{ij} of Cd₃As₂ in two samples (A4, A5) in “set A” and two samples (B10, B20) in “set B” with the applied thermal gradient $-\nabla T \parallel \hat{\mathbf{x}}$ and magnetic field $\mathbf{B} \parallel \hat{\mathbf{z}}$ (see Ref. [20] for details of the electrical transport measurements in set A and set B samples). We obtain S_{xx} and S_{xy} as

$$-S_{xx} = E_x / |\nabla T| = -(\rho_{xx} \alpha_{xx} + \rho_{yx} \alpha_{xy}) \quad (2)$$

$$S_{xy} = E_y / |\nabla T| = \rho_{xx} \alpha_{xy} - \rho_{yx} \alpha_{xx}, \quad (3)$$

where α_{ij} is the thermoelectric linear response tensor, and ρ_{ij} is the resistivity tensor (see Supplement for the details).

In Dirac semimetals, the AHE and ANE arise because the Berry curvature $\mathbf{\Omega}(\mathbf{k})$ imparts to the carriers an anomalous velocity $\mathbf{v}_A = \mathbf{\Omega}(\mathbf{k}) \times \hbar \dot{\mathbf{k}}$, i.e. $\mathbf{\Omega}(\mathbf{k})$ acts like an effective magnetic field in \mathbf{k} space ($\dot{\mathbf{k}}$ is the rate of change of the wavevector \mathbf{k}) [25]. Previously, the AHE was observed in Cd₃As₂ as a weak, low- B , anomaly in the Hall resistivity ρ_{yx} (Ref. [20]). The advantage of the Nernst effect is that it is more sensitive to the anomalous contributions [31–33]. This is because the thermoelectric signals are proportional to the derivative of the conductivities as given by the Mott relation [34], viz.,

$$\alpha_{ij} = \mathcal{A} \left[\frac{\partial \sigma_{ij}}{\partial \varepsilon} \right]_{\zeta}, \quad \left(\mathcal{A} = \frac{\pi^2 k_B^2 T}{3e} \right), \quad (4)$$

where k_B is Boltzmann’s constant, e the elemental charge and ζ the chemical potential.

In high-mobility semimetals, the conventional Nernst signal rises steeply to a sharp Drude-like peak at the peak field $B_p = 1/\mu$ (where μ is the mobility), and then

decreases towards zero when $B \gg 1/\mu$ (the “dispersive” field profile is well illustrated by the curves in Ref. [35]). By contrast, the ANE signal rises to a maximum value in weak B and remains pinned at this plateau value at large B ; its profile is step-like.

Figure 1 shows the measured Nernst signals at selected temperatures T in samples A4, A5, B10 and B20, respectively. The anomalous component is clearly evident in all 4 samples. The ANE in set A samples dominates the conventional Nernst effect at all T up to 200 K. By contrast, in set B samples, the conventional dispersive profile dominates the signal at high T , and the ANE only becomes prominent below 30 K. Theoretically, the separation of the conventional and anomalous contributions to the observed Nernst signal has not been solved in the high-field regime. As an empirical approach, we adopt the following expressions:

$$S_{xy} = S_{xy}^N + S_{xy}^A \quad (5)$$

$$S_{xy}^N = S_0^N \frac{\mu B}{1 + (\mu B)^2} \quad (6)$$

$$S_{xy}^A = \Delta S_{xy}^A \tanh(B/B_0). \quad (7)$$

Here, μ is the carrier mobility, S_0^N is the amplitude of the conventional semiclassical contribution S_{xy}^N (for details, see Ref. [35]), ΔS_{xy}^A is the amplitude of the anomalous Nernst signal S_{xy}^A , and B_0 is the saturation field above which the signal attains its plateau value ΔS_{xy}^A .

The empirical expressions provide good fits in all samples. Examples of the fits are shown for sample A4 in Fig. 2B. The amplitude ΔS_{xy}^A of the ANE derived from the fits is plotted in Fig. 2A. Interestingly, while the anomalous Nernst amplitude is small and nearly T independent in set B samples, it is large and strongly T -dependent in set A samples. The steep increase below ~ 50 K recalls the T dependence of the transport lifetime τ_{tr} in set A samples. This suggests a close relation between the ANE and the protection mechanism from backscattering implied by the ultrahigh mobility in set A samples ($\mu \sim 10^7$ cm² V⁻¹ s⁻¹; see Fig. 1 of Ref. [20] and Fig. 2).

Next, we discuss the thermopower S_{xx} . The measured signals in samples A4, B10 and B20 can be explained by the conventional semiclassical expression (see Ref. [35])

$$S_{xx}(B) = S_0 \frac{1}{1 + (\mu B)^2} + S_\infty \frac{(\mu B)^2}{1 + (\mu B)^2}. \quad (8)$$

Here, S_0 is the thermopower at $B = 0$ and S_∞ is the limiting value when $B \gg 1/\mu$. For samples A4 and B10, the fits are shown in Panels A, B of Fig. 3. (In sample A5, the ultrahigh mobility makes the observed thermopower harder to interpret).

As discussed, the splitting of each Dirac node into two Weyl nodes leads to a finite $\mathbf{\Omega}(\mathbf{k})$. In addition, separation of the Weyl nodes also produces a beating of the

bulk quantum oscillations which can be seen in the thermopower and Nernst effect (but are less evident in ρ_{ij} measured on the same samples [20]). Panel C of Fig. 3 plots the oscillatory part of the Nernst signals in samples A4, A5, B10 and B20. The beating effect is quite prominent. The macroscopic thickness of the samples (350-1460 μm) implies that the beating effect arises from interference of closely spaced oscillations in *bulk* states, rather than from surface states related to Fermi arcs. Panel D shows the index plots for the average frequency and the envelope frequency of the beating signal in sample A5. From the slope of the index plot, we extracted the values $S_F^{\text{ave}} = 42$ T and $S_F^{\text{env}} = 4.5$ T, from which we obtain two frequencies $S_1 = 46.5$ T and $S_2 = 37.5$ T differing by $\sim 20\%$. Similar values were found for samples A4 ($S_1 = 50.8$ T, $S_2 = 44.3$ T), B10 ($S_1 = 55.6$ T, $S_2 = 46.9$ T), B20 ($S_1 = 51$ T, $S_2 = 43$ T). The beating effect is consistent with the scenario in which the Dirac nodes split into Weyl nodes, leading to distinct Fermi surface cross-section areas.

We also investigated the magnetic response of Cd₃As₂ via torque magnetometry measurements on samples A4, A5, B10 and B20 (Fig. 4). Each of the samples, except for B10, shows an “anomalous magnetization” $M_\tau \equiv \tau/H$. This is quite surprising because Cd₃As₂ does not have magnetic elements. This raises the question whether the observed ANE is related to the “anomalous magnetization”. At first glance, the anomalous M_τ is reminiscent of conventional ferromagnetism. However, this scenario is easily excluded by comparing the data of M_τ taken via torque magnetometry with the magnetization data measured by regular SQUID magnetometry. Both the anomalous M_τ and the ANE signals are unchanged whether we cool in a finite field or in zero field (see Supplement). By contrast, the step-like magnetization observed in the SQUID data appears only when the sample is cooled in a finite field. To us, it is highly unlikely that the ANE arises from conventional ferromagnetism.

A second question is whether the anomalous M_τ is coming from the orbital magnetization [25, 36] generated by $\mathbf{\Omega}(\mathbf{k})$. If this is the case, the ANE and the “anomalous magnetization” should show the same dependences on both B and T . However, our experiments also exclude this scenario. In all samples, the anomalous M_τ is restricted to fields well below ~ 1 T at all T investigated (its magnitude which persists to 200 K is nearly T independent). By contrast, the magnitudes of the ANE increase rapidly below ~ 50 K in set A samples. The onset fields of the anomalous Nernst signals also increase up to $\gtrsim 5$ T at 200 K, in strong contrast with the behavior of M_τ . Finally, in sample B10, the ANE is finite whereas the anomalous M_τ signal is absent altogether. Therefore, we conclude that the ANE and the anomalous M_τ have very different origins (further discussion on this point is given in the Supplement).

In conclusion, we have performed a detailed investiga-

tion of the thermoelectric tensor in Cd_3As_2 for both set A and set B samples. The Nernst signals reveal a large ANE, suggestive of the existence of Berry curvature $\Omega(\mathbf{k})$ produced by separation of the Weyl nodes in applied \mathbf{B} . We also observe a significant beating effect in the quantum oscillations of the Nernst signals. The magnitude of the anomalous part of Nernst signals can be extracted via the phenomenological expressions Eqs. 5, 6, 7, whose temperature dependence in set A samples shows a rapid increase below ~ 50 K. The strong increase of τ_{tr} below 50 K suggests a close relation between the ANE and the mechanism that protects the carriers from backscattering.

-
- [1] Xiangang Wan, Ari M. Turner, Ashvin Vishwanath, and Sergey Y. Savrasov, “Topological semimetal and Fermi-arc surface states in the electronic structure of pyrochlore iridates,” *Phys. Rev. B* **83**, 205101 (2011).
- [2] S. M. Young, S. Zaheer, J. C. Y. Teo, C. L. Kane, E. J. Mele, and A. M. Rappe, “Dirac Semimetal in Three Dimensions,” *Phys. Rev. Lett.* **108**, 140405 (2012).
- [3] Kai-Yu Yang, Yuan-Ming Lu, and Ying Ran, “Quantum Hall effects in a Weyl semimetal: Possible application in pyrochlore iridates,” *Phys. Rev. B* **84**, 075129 (2011).
- [4] Chen Fang, Matthew J. Gilbert, Xi Dai, and B. Andrei Bernevig, “Multi-Weyl Topological Semimetals Stabilized by Point Group Symmetry,” *Phys. Rev. Lett.* **108**, 266802 (2012).
- [5] Shuichi Murakami, “Phase transition between the quantum spin Hall and insulator phases in 3D: emergence of a topological gapless phase,” *New Journal of Physics* **9**, 356 (2007).
- [6] Shuichi Murakami and Shun-ichi Kuga, “Universal phase diagrams for the quantum spin Hall systems,” *Phys. Rev. B* **78**, 165313 (2008).
- [7] Zhijun Wang, Yan Sun, Xing-Qiu Chen, Cesare Franchini, Gang Xu, Hongming Weng, Xi Dai, and Zhong Fang, “Dirac semimetal and topological phase transitions in $A_3\text{Bi}$ ($A = \text{Na}, \text{K}, \text{Rb}$),” *Phys. Rev. B* **85**, 195320 (2012).
- [8] Zhijun Wang, Hongming Weng, Quansheng Wu, Xi Dai, and Zhong Fang, “Three-dimensional Dirac semimetal and quantum transport in Cd_3As_2 ,” *Phys. Rev. B* **88**, 125427 (2013).
- [9] Su-Yang Xu, Chang Liu, Satya K. Kushwaha, Raman Sankar, Jason W. Krizan, Ilya Belopolski, Madhab Neupane, Guang Bian, Nasser Alidoust, Tay-Rong Chang, Horng-Tay Jeng, Cheng-Yi Huang, Wei-Feng Tsai, Hsin Lin, Pavel P. Shibayev, Fang-Cheng Chou, Robert J. Cava, and M. Zahid Hasan, “Observation of Fermi arc surface states in a topological metal,” *Science* **347**, 294–298 (2015).
- [10] L. X. Yang, Z. K. Liu, Y. Sun, H. Peng, H. F. Yang, T. Zhang, B. Zhou, Y. Zhang, Y. F. Guo, M. Rahn, D. Prabhakaran, Z. Hussain, S. K. Mo, C. Felser, B. Yan, and Y. L. Chen, “Weyl semimetal phase in the non-centrosymmetric compound TaAs,” *Nat Phys* **11**, 728–732 (2015).
- [11] B. Q. Lv, H. M. Weng, B. B. Fu, X. P. Wang, H. Miao, J. Ma, P. Richard, X. C. Huang, L. X. Zhao, G. F. Chen, Z. Fang, X. Dai, T. Qian, and H. Ding, “Experimental Discovery of Weyl Semimetal TaAs,” *Phys. Rev. X* **5**, 031013 (2015).
- [12] Philip J. W. Moll, Nityan L. Nair, Toni Helm, Andrew C. Potter, Itamar Kimchi, Ashvin Vishwanath, and James G. Analytis, “Transport evidence for Fermi-arc-mediated chirality transfer in the Dirac semimetal Cd_3As_2 ,” *Nature* **535**, 266–270 (2016).
- [13] Stephen L. Adler, “Axial-Vector Vertex in Spinor Electrodynamics,” *Phys. Rev.* **177**, 2426–2438 (1969).
- [14] J. S. Bell and R. Jackiw, “A PCAC puzzle: $\pi^0 \rightarrow \gamma\gamma$ in the σ -model,” *Il Nuovo Cimento A* (1965-1970) **60**, 47–61 (1969).
- [15] H.B. Nielsen and Masao Ninomiya, “The adler-bell-jackiw anomaly and weyl fermions in a crystal,” *Physics Letters B* **130**, 389 – 396 (1983).
- [16] D. T. Son and B. Z. Spivak, “Chiral anomaly and classical negative magnetoresistance of Weyl metals,” *Phys. Rev. B* **88**, 104412 (2013).
- [17] Jun Xiong, Satya K. Kushwaha, Tian Liang, Jason W. Krizan, Max Hirschberger, Wudi Wang, R. J. Cava, and N. P. Ong, “Evidence for the chiral anomaly in the Dirac semimetal Na_3Bi ,” *Science* **350**, 413–416 (2015).
- [18] Max Hirschberger, Satya K. Kushwaha, Zhijun Wang, Quinn Gibson, Sihang Liang, Carina A. Belvin, B. A. Bernevig, R. J. Cava, and N. P. Ong, “The chiral anomaly and thermopower of Weyl fermions in the half-Heusler GdPtBi ,” *Nat Mater* **15**, 1161–1165 (2016).
- [19] Heon-Jung Kim, Ki-Seok Kim, J.-F. Wang, M. Sasaki, N. Satoh, A. Ohnishi, M. Kitaura, M. Yang, and L. Li, “Dirac versus Weyl Fermions in Topological Insulators: Adler-Bell-Jackiw Anomaly in Transport Phenomena,” *Phys. Rev. Lett.* **111**, 246603 (2013).
- [20] Tian Liang, Quinn Gibson, Mazhar N. Ali, Minhao Liu, R. J. Cava, and N. P. Ong, “Ultrahigh mobility and giant magnetoresistance in the Dirac semimetal Cd_3As_2 ,” *Nat Mater* **14**, 280–284 (2015).
- [21] C. Zhang, E. Zhang, Y. Liu, Z.-G. Chen, S. Liang, J. Cao, X. Yuan, L. Tang, Q. Li, T. Gu, Y. Wu, J. Zou, and F. Xiu, “Detection of chiral anomaly and valley transport in Dirac semimetals,” *ArXiv e-prints* (2015), arXiv:1504.07698 [cond-mat.mtrl-sci].
- [22] Qiang Li, Dmitri E. Kharzeev, Cheng Zhang, Yuan Huang, I. Pletikoscic, A. V. Fedorov, R. D. Zhong, J. A. Schneeloch, G. D. Gu, and T. Valla, “Chiral magnetic effect in ZrTe_5 ,” *Nat Phys* **12**, 550–554 (2016).
- [23] C. Zhang, S.-Y. Xu, I. Belopolski, Z. Yuan, Z. Lin, B. Tong, N. Alidoust, C.-C. Lee, S.-M. Huang, H. Lin, M. Neupane, D. S. Sanchez, H. Zheng, G. Bian, J. Wang, C. Zhang, T. Neupert, M. Zahid Hasan, and S. Jia, “Observation of the Adler-Bell-Jackiw chiral anomaly in a Weyl semimetal,” *ArXiv e-prints* (2015), arXiv:1503.02630 [cond-mat.mes-hall].
- [24] Di Xiao, Yugui Yao, Zhong Fang, and Qian Niu, “Berry-Phase Effect in Anomalous Thermoelectric Transport,” *Phys. Rev. Lett.* **97**, 026603 (2006).
- [25] Di Xiao, Ming-Che Chang, and Qian Niu, “Berry phase effects on electronic properties,” *Rev. Mod. Phys.* **82**, 1959–2007 (2010).
- [26] Pavan Hosur and Xiaoliang Qi, “Recent developments in transport phenomena in Weyl semimetals,” *Comptes Rendus Physique* **14**, 857 – 870 (2013).
- [27] Rex Lundgren, Pontus Laurell, and Gregory A. Fiete,

- “Thermoelectric properties of Weyl and Dirac semimetals,” *Phys. Rev. B* **90**, 165115 (2014).
- [28] Girish Sharma, Pallab Goswami, and Sumanta Tewari, “Nernst and magnetothermal conductivity in a lattice model of Weyl fermions,” *Phys. Rev. B* **93**, 035116 (2016).
- [29] G. Sharma, C. Moore, and S. Tewari, “Nernst effect in topological Dirac semimetals,” *ArXiv e-prints* (2016), arXiv:1605.00299 [cond-mat.str-el].
- [30] B. Z. Spivak and A. V. Andreev, “Magnetotransport phenomena related to the chiral anomaly in Weyl semimetals,” *Phys. Rev. B* **93**, 085107 (2016).
- [31] Kamran Behnia, Marie-Aude Méasson, and Yakov Kopelevich, “Oscillating Nernst-Ettingshausen Effect in Bismuth across the Quantum Limit,” *Phys. Rev. Lett.* **98**, 166602 (2007).
- [32] Zengwei Zhu, Benoît Fauqué, Yuki Fuseya, and Kamran Behnia, “Angle-resolved Landau spectrum of electrons and holes in bismuth,” *Phys. Rev. B* **84**, 115137 (2011).
- [33] Zengwei Zhu, Xiao Lin, Juan Liu, Benoît Fauqué, Qian Tao, Chongli Yang, Youguo Shi, and Kamran Behnia, “Quantum Oscillations, Thermoelectric Coefficients, and the Fermi Surface of Semimetallic WTe_2 ,” *Phys. Rev. Lett.* **114**, 176601 (2015).
- [34] J. M. Ziman, “Electrons and Phonons (Oxford Clarendon Press, Oxford, 1960)p 500.” .
- [35] Tian Liang, Quinn Gibson, Jun Xiong, Max Hirschberger, Sunanda P. Koduvayur, R.J. Cava, and N.P. Ong, “Evidence for massive bulk Dirac fermions in $Pb_{1-x}Sn_xSe$ from Nernst and thermopower experiments,” *Nat Commun* **4**, – (2013).
- [36] Yu.N. Obraztsov, “Thermomagnetic phenomena in metals and semiconductors in quantizing (strong) magnetic fields,” *Sov. Phys. Solid State* **6**, 331–336 (1964).
- [37] See Supplemental Material, which includes Refs. [25, 34, 36, 38-39]
- [38] P. W. Bridgman, “The Connections between the Four Transverse Galvanomagnetic and Thermomagnetic Phenomena,” *Phys. Rev.* **24**, 644–651 (1924).
- [39] Yayu Wang, Lu Li, and N. P. Ong, “Nernst effect in high- T_c superconductors,” *Phys. Rev. B* **73**, 024510 (2006).

*These authors contributed equally to this work.

†Current address of T.L.: Department of Applied Physics, Stanford University, Stanford, CA, 94305

Acknowledgements T.L. acknowledges a scholarship from Japan Student Services Organization. N.P.O. acknowledges the support of the Gordon and Betty Moore Foundation’s EPiQS Initiative through Grant GBMF4539. R. J. C. and N. P. O. acknowledge support from the U.S. National Science Foundation (MRSEC Grant DMR 1420541).

Author Information The authors declare no competing financial interests. Correspondence and requests for data and materials should be addressed to T.L. (liang16@stanford.edu) or N.P.O. (npo@princeton.edu).

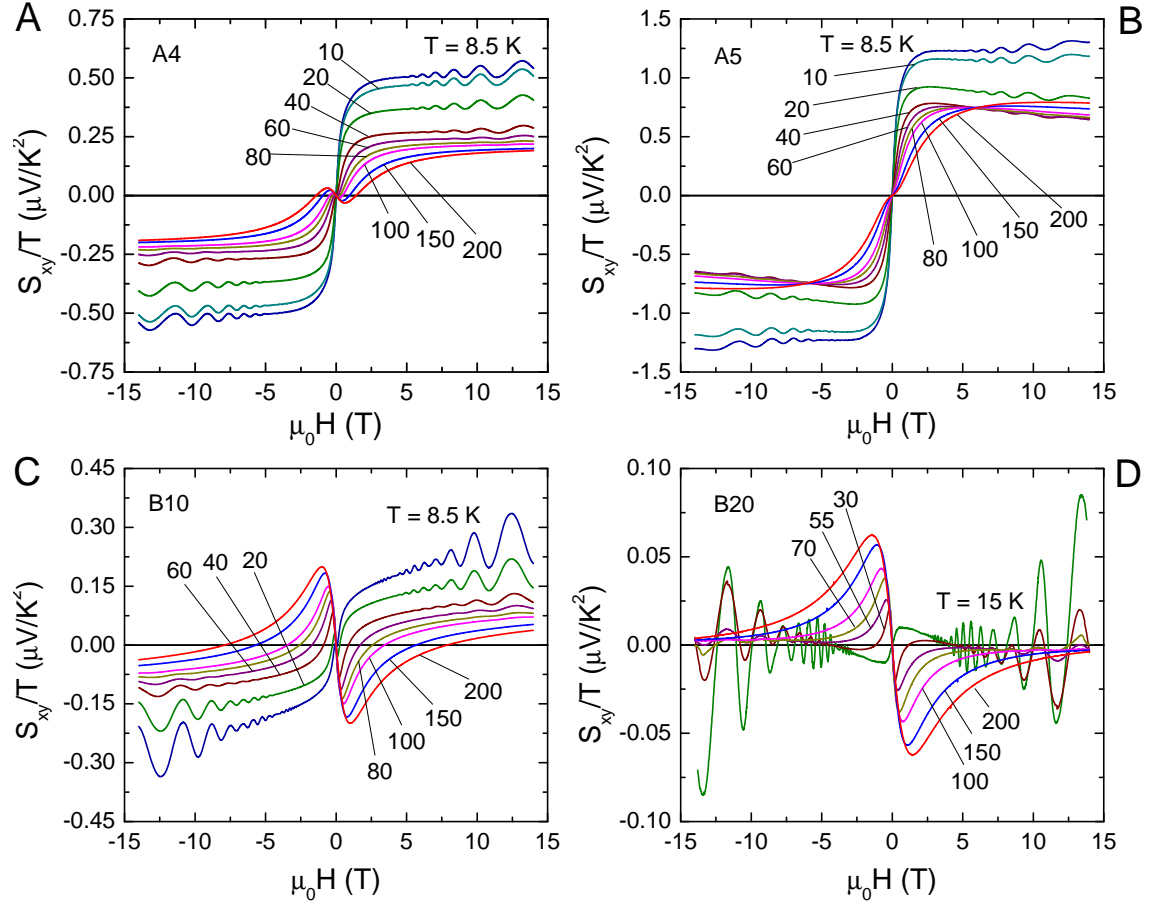


FIG. 1. (color online) Curves of the Nernst effect at selected temperatures T in samples A4 (Panel A), A5 (Panel B), B10 (Panel C), and B20 (Panel D). In each sample, the ANE component has a step-like profile (especially prominent in Panels A and B), whereas the conventional contribution shows a dispersive (Drude-like) peak (more evident in Panels C and D). In the set A samples A4 and A5, the ANE signal persists to 200 K. By contrast, in set B samples B10 and B20, the conventional Drude-like Nernst signal dominates except at low T (< 30 K) where the ANE dominates.

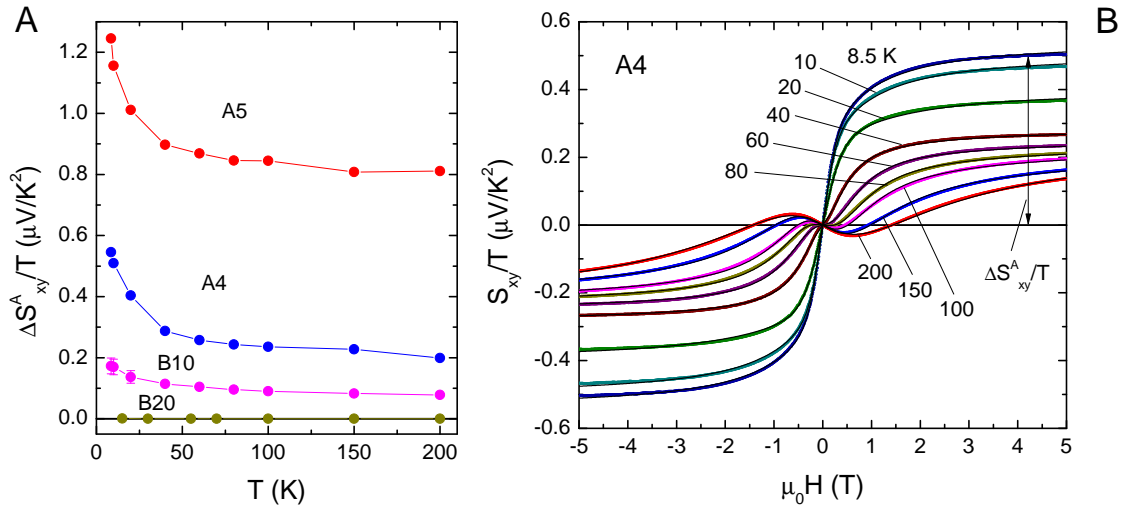


FIG. 2. (color online). Panel A: The temperature dependence of the amplitude of anomalous Nernst signal $\Delta S_{xy}^A/T$. In the set A samples A4 and A5, the magnitude of anomalous Nernst signals develops rapidly below 50 K, suggestive of a correlation with the mechanism that protects carriers against backscattering. Panel B: Fits to the observed Nernst effect in sample A4. The observed Nernst effect was fitted to the empirical expression $S_{xy} = S_0^N \mu B / (1 + (\mu B)^2) + \Delta S_{xy}^A \tanh(B/B_0)$, where S_0^N and ΔS_{xy}^A represent the amplitude of normal and anomalous part of Nernst signals, respectively (Eqs. 5, 6, 7). The expression provides good fits (black curves) to the data.

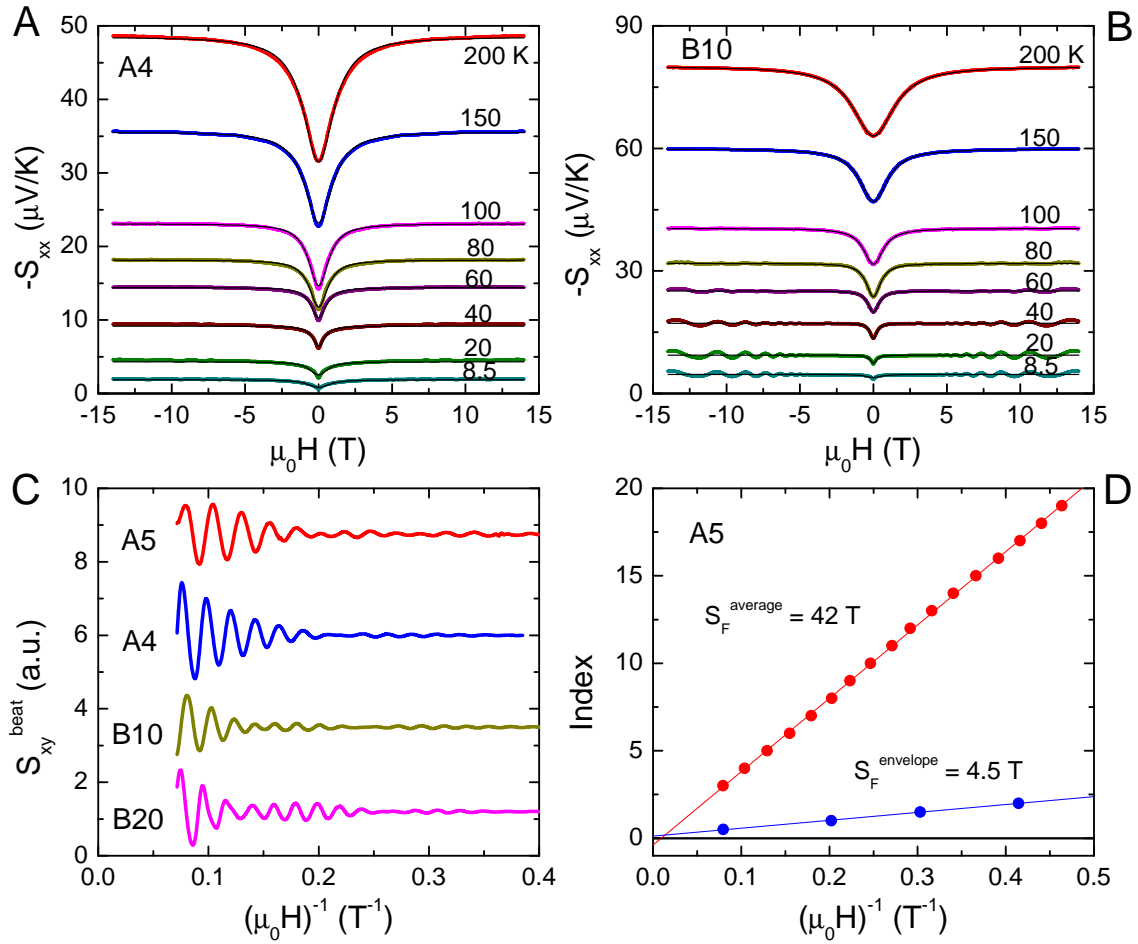


FIG. 3. (color online). Beating pattern in the quantum oscillations in the Nernst signals. Panels A and B show the Seebeck signals of sample A4 (left panel) and B10 (right panel) at selected T . The Seebeck signals can be fit using semiclassical expression in Eq. 8. Panel C shows the oscillatory part of the Nernst signals in each sample. Clear beatings were observed for every sample, suggestive of the splitting of Dirac nodes into Weyl nodes. Panel D shows the index plot for sample A5 which determines the two Fermi surface areas $S_1 = 46.5$ T and $S_2 = 37.5$ T.

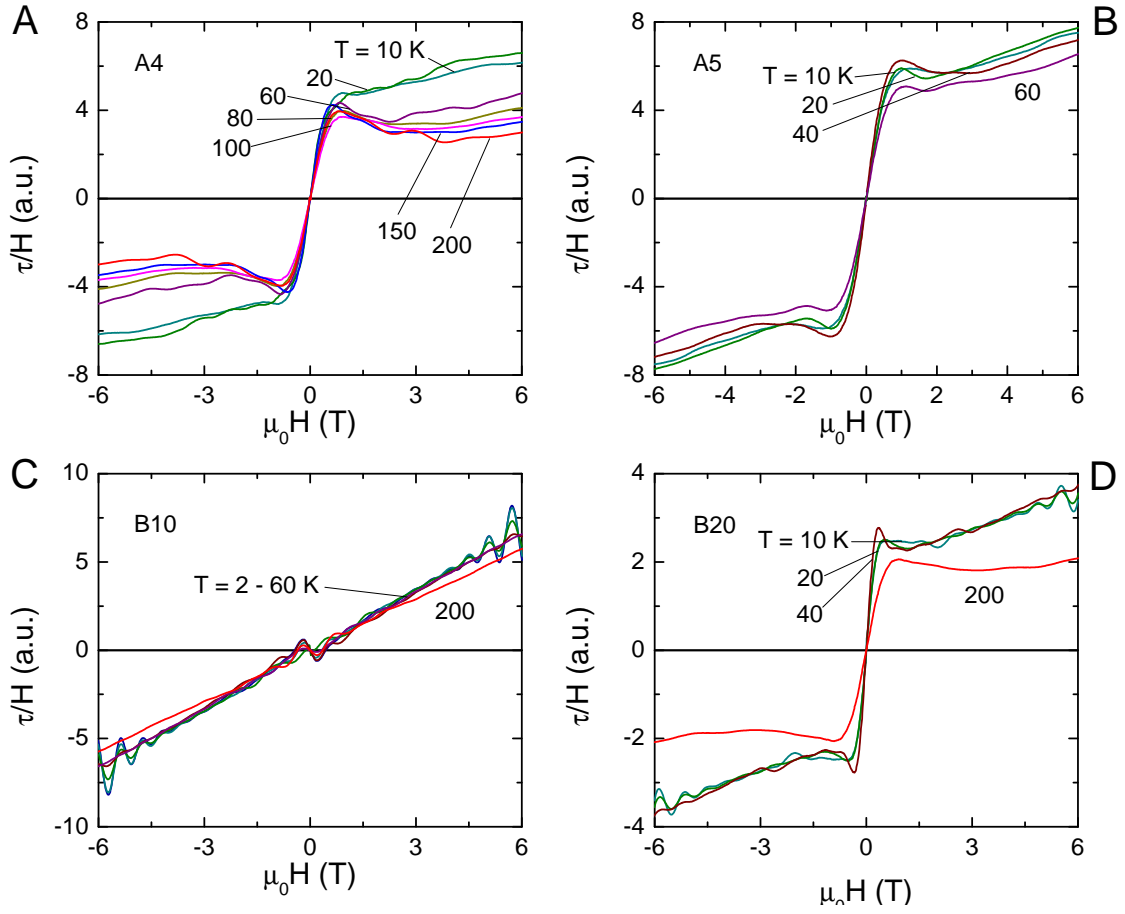


FIG. 4. (color online). “Anomalous magnetization” $M_\tau \equiv \tau/H$ at selected T obtained from torque magnetometry in samples A4, A5, B10 and B20. The anomalous part is confined to B below 1 T in all samples at all T investigated, with a nearly T -independent magnitude. These characteristics distinguish M_τ from the ANE signals in Fig. 1, and imply that M_τ has a different origin from the ANE.